Flexible and Wireless Multi-Point Epidermal Temperature Sensor

Nicoletta Panunzio, *Student Member, IEEE,* Arianna Diamanti, and Gaetano Marrocco, *Senior Member, IEEE*

***Abstract*—Measurement of body temperature is the most frequent medical screening performed in both hospital and domestic environments. Dual-heat-flux (DHF) thermometry provides an indirect method to estimate deep body temperature, which is unpractical and uncomfortable to be measured, from the easily accessible surface of the skin, by exploiting four temperature sampling points on a same device. This paper combines, for the first time, the DHF method with the flexible epidermal Ultra High Frequency (UHF) Radio Frequency IDentification (RFID) technology to replace bulky and wired state-of-the-art DHF devices. Four RFID Integrated Circuits (ICs) with embedded temperature sensors are used in place of the wired temperature probes so that they will be in charge of both sensing and wireless transmission of the data by means of four small antennas also embedded in the device. By integrating the antennas within elastomeric substrates, a highly conformable plaster-like device is achieved. It is flexible and soft, and can be read from a distance of more than $15\,cm$ regardless of the curvature of the body region where it is placed, and also in case of moderate displacement ($\pm 5\,cm$) with respect to the external interrogator.**

***Index Terms*—epidermal antenna, Radio Frequency Identification (RFID), core body temperature, multichip, dual-heat-flux model, flexible sensor**

I. Introduction

MEASUREMENT of body temperature is the most frequent medical screening to trace the state of health of a person [1]. A reliable evaluation of core temperature (i.e., that of organs) requires invasive measurements through the insertion of thermal probes inside specific anatomical body districts (e.g., mouth, ear, rectum) [2]. Temperature measurements over the skin, instead, are practical and non-invasive [2]. Accordingly, the indirect monitoring of deep body temperature from the surface of the skin is desirable. However, skin and core temperatures are not linearly correlated [3], so that *ad-hoc* models should be involved to derive the deep temperature from surface measurements.

For this purpose, dual-heat-flux (DHF) thermometry was firstly introduced in [4] as a method to estimate core temperature from the surface of the skin by means of a four-sensor layered device (Fig. 1). Over the years, many efforts have been made to increase the accuracy and precision of the method by exploiting different insulating materials for the layers [5], [6] (e.g., rubber, nylon, polystyrene, PDMS) as well as different form factors [7], [8] (e.g., cylindrical, cuboid, truncated cone). However, all the proposed devices are still either wired or battery-dependent, unpractical, and sometimes rigid. Indeed, the state-of-the-art DHF thermometers involve traditional wired measurement systems [4], [9], are quite uncomfortable, and bulky (e.g., surface and thickness up to $15\,cm^2$ and $1.5\,cm$, respectively). Thereby, two main issues that limit the practical applicability of DHF thermometers are still open and not addressed: the lack of flexibility and the presence of wired or battery-driven sensors.

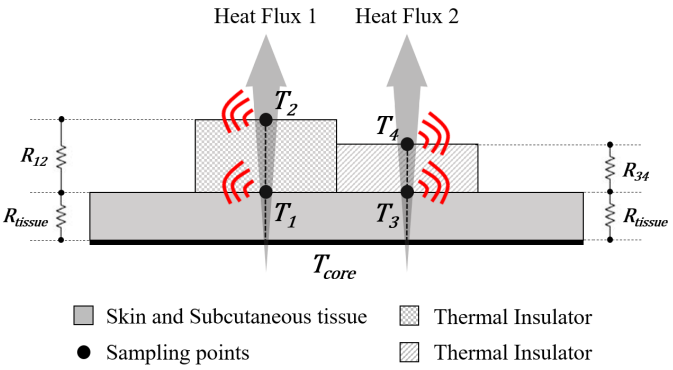

Fig. 1. Concept of dual-heat-flux epidermal thermometer integrating the RFID technology for temperature data acquisition and transmission.

To make the transmission of the temperature data wireless, we propose a novel approach to combine, for the first time, the DHF method with the flexible epidermal Ultra High Frequency (UHF) Radio Frequency IDentification (RFID) technology [10]. Indeed, UHF RFID epidermal sensors have notably increased their real-world applicability in recent years for the wireless and non-invasive measurement of skin parameters, and temperature above all [11], [12]. Typical epidermal RFID temperature sensors are suitable to be directly attached to the human skin by means of biocompatible transpiring membranes that support or enclose a battery-less compact antenna [13]. A wide range of configurations exists: extremely miniaturized [11] or highly flexible [14] depending on the selected substrates for the specific application. The resulting epidermal devices can enable reading of skin temperature from a distance of a few centimeters [15] up to $1.5\,m$ [14]. Since many RFID ICs [16], [17] are now capable of both temperature sensing (by means of an embedded temperature sensor) and wireless data transmission (by means of typical RFID backscattering modulation), the electronic complexity and footprint of the resulting devices can be notably reduced as the addition of external temperature sensors can be avoided.

By exploiting the same approach, the idea of this paper is to replace the four temperature probes of the DHF thermometer with four sensing-oriented RFID ICs (Fig. 1) which are inte-

Manuscript received ; revised . The work was developed in the framework of the Dual-Skin project, funded by Italian Ministry of University and Research (FISR 2020 COVID, Ref. FISR2020IP 00227).

The authors are with the Pervasive Electromagnetics Lab, University of Rome Tor Vergata, Via del Politecnico 1, Rome, Italy (e-mail: nicoletta.panunzio@uniroma2.it, gaetano.marrocco@uniroma2.it).

grated within skin-friendly soft and flexible substrates. Thus, a low-profile soft device can be achieved, whose size is notably reduced with respect to the state-of-the-art. It will be fully wireless since it does not require batteries and wired power sources. Only small embedded antennas will be involved in the wireless transmission of the temperature data and multiple layers of biocompatible substrates will be exploited as the insulating layers of the DHF sensor [18] to ease the comfort and flexibility and to ensure biocompatibility.

A first demonstration of an on-skin antenna with a dual-temperature-probe was given in [12]. The device involved a square loop fed via two T-match transformers. It was non-uniformly coated by insulating layers. Two orthogonal backscattering modes were accordingly generated to collect two independent temperature data (i.e., skin and environment). This approach is suitable to enable a *multi-parametric sensing* [19], for which all the ports operate independently and each one returns meaningful data (e.g., temperature or other). However, as the two ICs in [12] were placed far from each other, this arrangement is unsuitable for capturing the heat flux. Indeed, the DHF method, which is a *single-parameter sensing* approach [19], requires that the sampling points are placed one over the other and that all the four ports coherently contribute to a single output data (i.e., the core temperature). Therefore, a different antenna configuration specifically hosting four ICs must be considered.

A preliminary feasibility demonstration of the RFID-based flexible and wireless DHF sensor was presented in the conference contributions [18], [20] by using non-optimized antennas as the unit radiating elements. To the best of our knowledge, it was the first implementation of an RFID sensor having *four* sampling probes closely stacked in the limited space of a flexible epidermal device. However, the effect of flexibility at the expense of the electromagnetic performance was not yet addressed, whereas, instead, a change in the relative position between the four antennas inside the device can have an impact on the wireless communication.

By extending the preliminary ideas of the conference contributions [18], [20], this paper faces the two main novelties of the proposed RFID-based DHF thermometer with respect to the state-of-the-art, that are the wireless transmission of the temperature data and the flexibility and conformability of the device. In particular, this paper is focused on the characterization of the robustness of the wireless data transmission, with also emphasis on the impact of the device curvature on the communication performance.

The paper is organized as follows. Section II introduces the statement of the problem by defining the layout of the flexible and wireless DHF device, the methods exploited during the design phase, as well as the electromagnetic metrics used for the numerical parametric analysis described in Section III. To reduce computational time and complexity, the selected radiating elements are firstly optimized one by one (Section III-A) and then verified in the four-antenna arrangement (Section III-B). A prototype is then fabricated by exploiting a *trim-and-transfer* manufacturing technique as outlined in Section IV. Finally, the experimental characterization tests in Section V are focused on the assessment of the electromagnetic performance, also to evaluate both the effects of device flexibility (Section V-B) and device-reader misalignment (Section V-C), as well as its sensing-oriented usability (Section V-D).

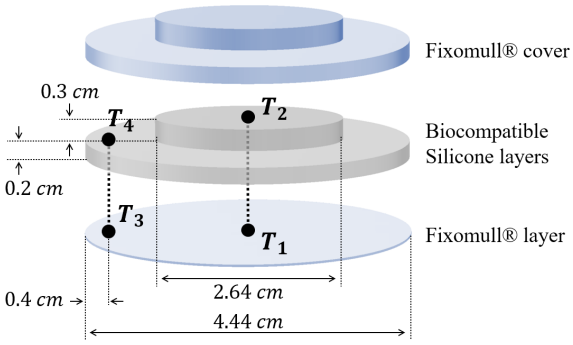

Fig. 2. Architecture of the multi-point epidermal temperature sensor.

II. Statement of the Problem

A. Rationale of the Dual-Heat-Flux Thermometry

Following the DHF model [4], four temperature sampling points on the same device need to be placed in pairs, one above the other (Fig. 1). The two temperature sensors closest to the skin are separated from the other couplet by means of thermal insulators having different thermal resistances. In this way, two simultaneous heat-flux paths are identified, coming from the inside of the body to the outside. The four temperatures can be combined to estimate [4] the core body temperature by merging the Fourier's laws of each path:

$$T_{core}^{est} = T_1 + \frac{(T_1 - T_2)(T_1 - T_3)}{K(T_3 - T_4) - (T_1 - T_2)}\,. \tag{1}$$

This estimation only depends on the four measured temperatures $T_{1\text{-}4}$ at different planes, as well as on the thermal resistances of the insulators by means of the parameter $K = R_{12}/R_{34}$, in which R_{12} and R_{34} are the thermal resistances between the two pairs of vertical probes, that can be assumed as known.

B. Layout of the DHF Flexible and Wireless Device

The cylindrical shape proposed in [21] was borrowed for the geometric layout of the device, as well as the positions of the temperature probes. The device (Fig. 2) is indeed made up of two cylindrical layers of insulating materials, whereas the four temperature probes are arranged in pairs, one pair in the center and the other $0.4\,cm$ from the outer edge (Fig. 2). The thicknesses of the layers were derived in [18] as a result of parametric thermal simulations.

The core substrates of the device are of biocompatible silicone ($\varepsilon_r = 2.2$, $\sigma = 0.005\,S/m$, $k = 0.02\,W/mK$, $\epsilon = 0.95$)[1], that can ensure flexibility and biocompatibility while having desired thermal properties (as assessed in [18]). A $220\,\mu m$ thick adhesive polyester non-woven sterile medical-grade fabric plaster (BSN Medical, Fixomull® Stretch, $\varepsilon_r =$

[1] ε_r: relative dielectric constant, σ: electrical conductivity, k: heat conductivity, ϵ: emissivity.

1.001, $\sigma = 0.005\,S/m$, $k = 0.04\,W/mK$, $\epsilon = 0.75$) is used for encapsulation. This material is indeed placed on top of the overall device as an external coating, ensuring a comfortable and robust bond with the skin, as well as below, to separate the metal traces of the antennas from the skin. The polyester fabric is particularly suitable for on-skin applications since it has a moisture regain of 0.2% at $65\%\,RH$ [22] (recommended value is below 3% [23]). Hence, this substrate is almost insensitive to the changes in the ambient relative humidity and, above all, to the absorption of sweat. Evidence of this can be found in [11].

Since the four sampling points (i.e., the sensing-oriented ICs) are separated and should lie on different planes (Fig. 2), each IC must be associated with an antenna for communication. The selected elementary radiating element is a circular loop (Fig. 3.a) since it can be parameterized by just two degrees of freedom: the diameter D and the trace width w. The latter is however fixed at $0.15\,cm$ to ease fabrication. The four loops are then arranged as in [20] to comply with the fixed positions of the temperature IC-probes, so that the resulting electromagnetic layout of the four-antenna device is as in Fig. 3.b,c.

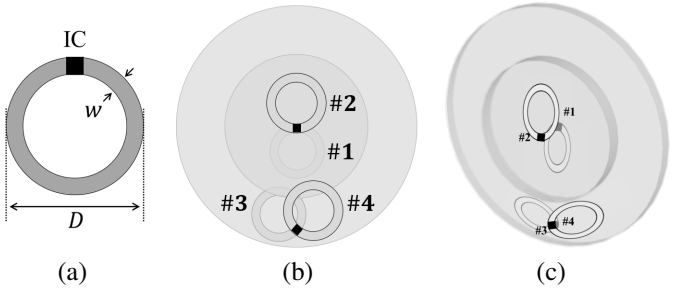

Fig. 3. (a) Circular loop antenna as the unit radiating element. (b,c) Electromagnetic layout of the four-antenna device.

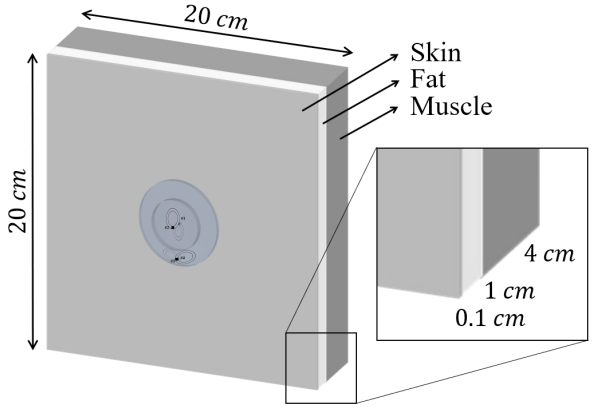

Fig. 4. Layered human phantom for numerical simulations.

C. Design Method

Numerical simulations based on the Finite Element Method (FEM) were performed by CST Microwave Studio over a $20\,cm \times 20\,cm$ electromagnetic layered numerical phantom (Fig. 4) made by skin ($\varepsilon_r = 54.5$, $\sigma = 0.6\,S/m$), fat ($\varepsilon_r = 5.64$, $\sigma = 0.1\,S/m$), and muscle ($\varepsilon_r = 54.5$, $\sigma = 0.6\,S/m$).

Without loss of generality, the following antenna optimization is referred to the Magnus-S3 microchip transponder by Axzon [16], embedding a solid-state temperature sensor[2]. The sensing-oriented chip sensitivity is $p_{chip} = -13\,dBm$. The IC is also provided with *auto-tuning* technology [25] that automatically adjusts the IC internal impedance to maximize the wireless power transfer. This feature is significantly convenient for on-body antennas as possible mismatches due to human body variability can be compensated for, so that the antenna performance is preserved in a wide frequency band.

To reduce computational time and complexity, the design method consisted of two steps. *(i)* The selected radiating elements were firstly optimized one by one as stand-alone antennas within the layered device, and then *(ii)* they were arranged in the final four-antenna configuration for the evaluation of the overall performance. For this purpose, the formalism for multi-port systems of coupled antennas [26], [27] was exploited. Accordingly, the parameter to be evaluated was the embedded realized gain $\tilde{G}_\tau^{(n)}$ of each port, expressed as in [28], that is the gain of each antenna scaled by the impedance mismatch with its *auto-tuning* IC [25].

The realized gain directly affects the maximum activation distance of each port and hence the readability of each temperature probe:

$$d_{max}^{(n)} = \frac{\lambda}{4\pi}\sqrt{\frac{EIRP\,\tilde{G}_\tau^{(n)}\,\eta_p}{p_{chip}}}\,. \tag{2}$$

η_p is the polarization loss factor, that takes into account the polarization mismatch between the sensor antenna and the interrogating antenna, and $EIRP$ is the Effective Isotropic Radiated Power emitted by the reader antenna. To be conservative, $\eta_p = 0.5$ will be assumed for all the following analyses, whereas the maximum power of $3.2\,W$ $EIRP$ allowed by European regulations [29] will be considered for the reader antenna.

The realized gain is also directly related to the turn-on power, that is the power emitted by the transmitter when the power collected by the n-th antenna equals the chip sensitivity p_{chip}:

$$P_R^{TO\,(n)} = \eta_p \left(\frac{4\pi d}{\lambda}\right)^2 \frac{p_{chip}}{G_R\,\tilde{G}_\tau^{(n)}}\,, \tag{3}$$

where G_R is the radiation gain of the reader antenna and d its distance from the sensor antennas. The turn-on power is easily measured experimentally as the minimum power that the transmitter must emit to make each antenna respond. The exceeding power that can be provided represents instead the power margin (in dB):

$$M^{(n)} = 30\,dBm - P_R^{TO(n)}\,, \tag{4}$$

being $30\,dBm$ the maximum output power from the reader. Finally, it is worth noticing that an inverse proportionality

[2]Operation range: $[-40,\,85]°C$ [16]. Resolution: $0.13°C$ [16]. Accuracy and precision for body temperature measurement: $0.2°C$ [24].

exists between the turn-on power and the realized gain, that is $P_R^{TO\,(n)} = k - \tilde{G}_\tau^{(n)}$ (in decibel), being k a fixed constant once fixed the measurement setup.

D. Metrics for the Multi-port Antenna Evaluation

The reliability and robustness of the four-port device are related to the capability of simultaneously reading the four ICs, possibly regardless of the interrogation angle. Accordingly, the device will be characterized in simulations by the following two metrics defined in terms of realized gains.

1) Inter-IC Uniformity U_{IC}, defined by this hollow diagonal symmetric matrix:

$$U_{IC} = \begin{bmatrix} 0 & \Delta\tilde{G}_\tau^{(1,2)} & \Delta\tilde{G}_\tau^{(1,3)} & \Delta\tilde{G}_\tau^{(1,4)} \\ & 0 & \Delta\tilde{G}_\tau^{(2,3)} & \Delta\tilde{G}_\tau^{(2,4)} \\ & & 0 & \Delta\tilde{G}_\tau^{(3,4)} \\ & & & 0 \end{bmatrix}, \tag{5}$$

where the (n, m) entry quantifies the *differential realized gain* between two antennas:

$$\Delta\tilde{G}_\tau^{(n,m)} = |\, av(\tilde{G}_\tau^{(n)}) - av(\tilde{G}_\tau^{(m)})|\,, \tag{6}$$

being $av(\tilde{G}_\tau^{(i)})$ the broadside realized gain in dBi of the i-th port averaged over the European UHF band. The smaller $\Delta\tilde{G}_\tau^{(n,m)}$, the strongest is the symmetry between the antennas. Anyways, the gain of the less-performing antenna must be considered as the bottleneck to define the overall communication performance.

2) Angular Uniformity $U_{\underline{\hat{r}}}^{(n)}$, defined as the *angular variance* of the realized gain for each n-th antenna:

$$U_{\underline{\hat{r}}}^{(n)} = \frac{1}{N-1} \sum_{m=1}^{N} |\, \tilde{G}_\tau^{(n)}(\underline{\hat{r}}_m) - \mu^{(n)} \,|^2\,, \tag{7}$$

where N is a discrete set of observation angles in the front half-space of the device, opposite to the body, that are identified by the unit vector $\underline{\hat{r}}$, $\tilde{G}_\tau^{(n)}(\underline{\hat{r}}_m)$ is the realized gain in dBi of the n-th antenna for each selected direction of observation $\underline{\hat{r}}$, and $\mu^{(n)}$ is the mean of $\tilde{G}_\tau^{(n)}(\underline{\hat{r}}_m)$:

$$\mu^{(n)} = \frac{1}{N} \sum_{m} \tilde{G}_\tau^{(n)}(\underline{\hat{r}}_m)\,. \tag{8}$$

The less the variance $U_{\underline{\hat{r}}}^{(n)}$, the more the angular performance is uniform, which guarantees smoother readability.

It is worth noticing that, since the two metrics perform a difference in dBi between realized gains, their value can be equivalently computed in measurements in terms of turn-on powers, returning the same result.

III. Numerical Analysis

A. Parametric Analysis of Stand-Alone Antennas

Fig. 5 shows the realized gains of the loops by varying the external diameter D. The minimum size compatible to mount the IC is $D = 0.9\ cm$. The maximum diameters, instead, are fixed for each position so that the antenna can fit inside the edges of the silicone layers. The numerical

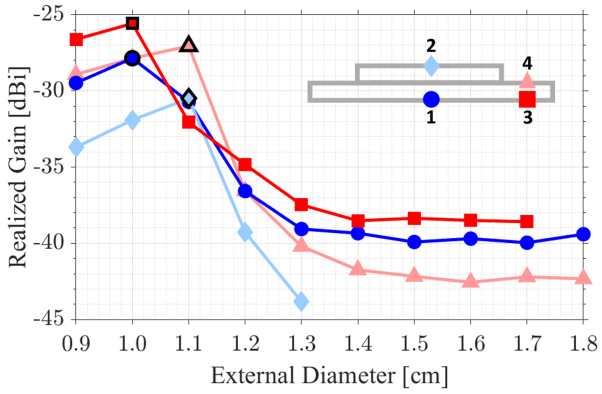

Fig. 5. Parametric analysis to optimize the external diameter of each loop antenna in terms of the realized gain. Fixed frequency of 870 MHz.

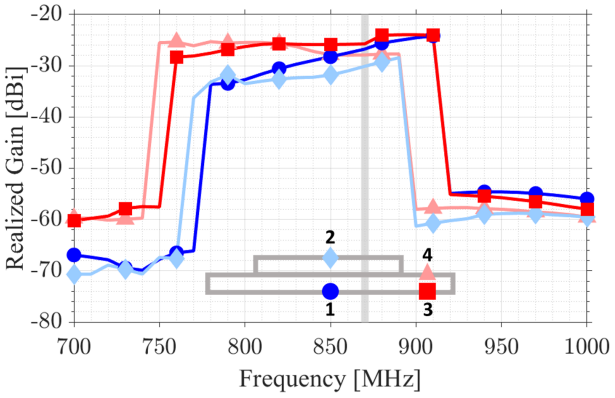

Fig. 6. Simulated trends of the broadside realized gains over frequency of the four antennas of the device. Shadowed, the European UHF band.

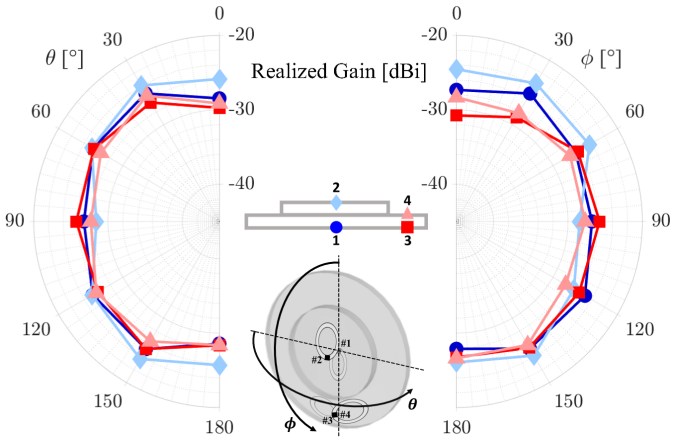

Fig. 7. Simulated realized gains of the four antennas over two orthogonal cuts crossing the center of the device. Frequency fixed at 870 MHz.

results show that two pairs of antennas with slightly different diameters (i.e., $1.0\,cm$ and $1.1\,cm$) are enough to achieve the maximum response in all positions, for which the four loops have comparable performance: $-30\,dBi < \tilde{G}_\tau^{(n)} < -25\,dBi$. These limited achievable values are due to the small size of the loop antennas as well as the presence of lossy biological tissues.

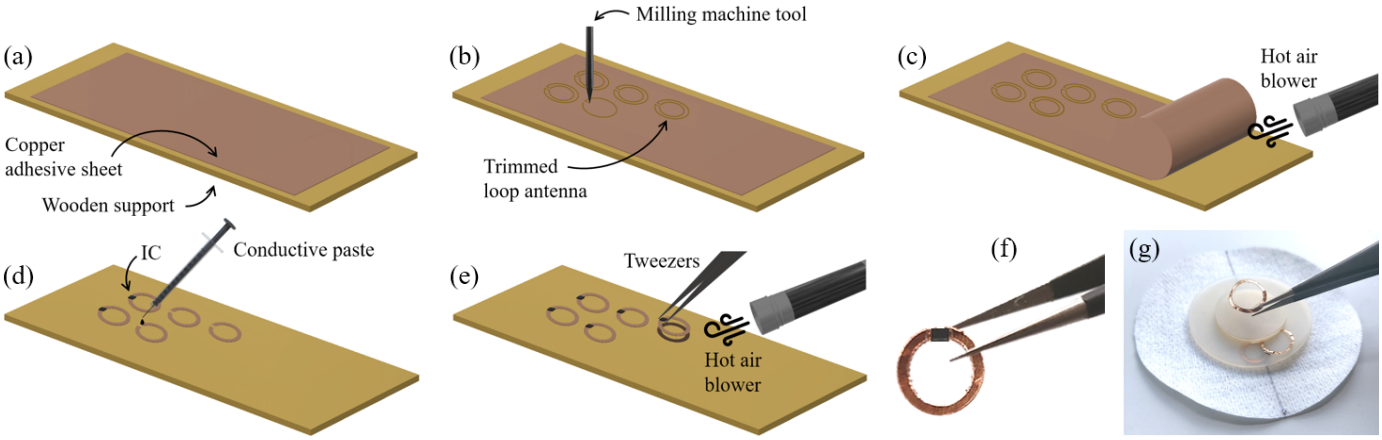

Fig. 8. *Trim-and-transfer* fabrication technique. (a) Deposition of a copper adhesive sheet over a wooden support. (b) Trimming of the loop antennas by using a milling machine. (c) Thermally-induced removal of extra copper. (d) Soldering of ICs by using conductive paste. (e) Thermally-induced releasing of the antennas. (f) Resulting loop antenna (g) transferred to the flexible substrate.

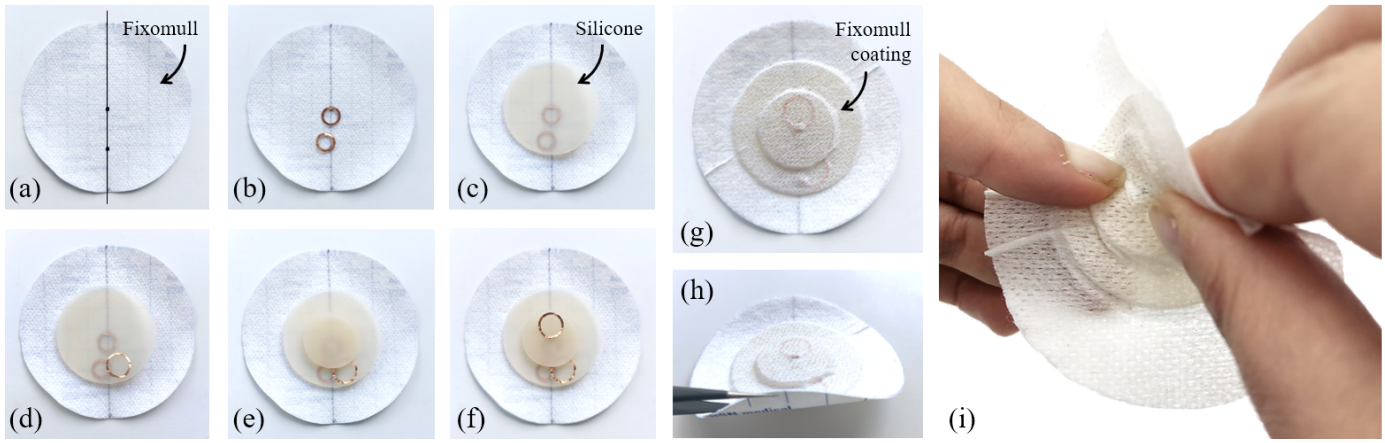

Fig. 9. (a-f) Manufacturing steps for prototyping the flexible epidermal multi-point RFID thermometer. (a) Fixomull® plaster disc laid over the workbench with the non-adhesive side facing upward; main axis of the device and the position of the two pairs of ICs indicated as a guide. (b) Deposition of antennas #1 and #3, with ICs facing downward. (c) Deposition of the $2\,mm$ thick silicone substrate. (d) Deposition of antenna #4. (e) Deposition of the $3\,mm$ thick silicone substrate. (f) Deposition of antenna #3. (g) Whole layers covered with Fixomull® plaster with the adhesive side facing downward. (g-h) Final prototype of the multi-point RFID thermometer. (i) Evidence of the flexibility of the device.

B. Four-Antenna Configuration

The four-antenna device was then put together as in Fig. 3.b,c. The simulated realized gains over frequency are shown in Fig. 6, whose trends are peculiar due to the auto-tuning that widens the frequency band in which the performance is stable.

The evaluation of the inter-IC uniformity metrics by (5) at 870 MHz returns:

$$U_{IC} = \begin{bmatrix} 0 & 3.3 & 1.1 & 1.1 \\ & 0 & 4.4 & 2.2 \\ & & 0 & 2.2 \\ & & & 0 \end{bmatrix} dBi\,. \tag{9}$$

The highest contrast (i.e., $\Delta\tilde{G}_\tau^{(2,3)} = 4.4\,dBi$) is between antenna #2 and #3, that indeed see the most different boundary conditions. Instead, antenna #1 has similar performance to both antennas #3 and #4 (i.e., $\Delta\tilde{G}_\tau^{(1,3)}, \Delta\tilde{G}_\tau^{(1,4)} = 1.1\,dBi$), that yet are the closer to the skin. Accordingly, by computing (2) for the worst performing antenna (i.e., #2), it follows that all the four temperature sensors will be read from a maximum distance of $15\,cm$.

Concerning the angular response of the device, the polar plots in Fig. 7 show that the patterns are rather uniform over two orthogonal cuts crossing the center of the device. This is confirmed by the angular variances computed as in (7), that return $U_{\underline{\hat{r}}}^{(n)} = \{0.5,\, 2.5,\, 1.1,\, 1.0\}\,dBi$, for $n = \{1,\, 2,\, 3,\, 4\}$ respectively. This means that the expected read distance is greater than $10\,cm$ even if the device is read from the edge of the skin. Hence, it could be compatible with an interrogation by a close-by on-body reader, for example, embedded within garments at the chest level.

IV. Prototype

A. Fabrication

The sheets of biocompatible substrates used to manufacture the device were carved out using a circular hollow cutter with different diameters. The circular loop antennas, instead, were manufactured by means of a *trim-and-transfer* fabrication

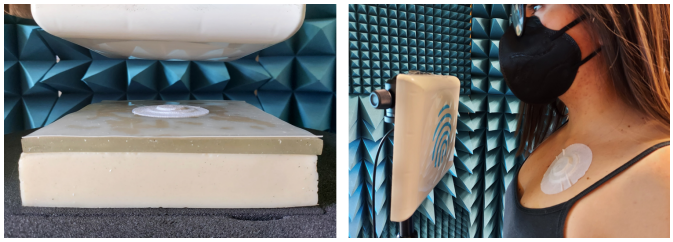

(a) (b)

Fig. 10. Measurement setup in a semi-anechoic room. CP reader antenna at fixed distance of 10 cm. (a) Prototype attached on a semi-solid three-layers phantom. (b) Volunteer wearing the device on the chest.

technique (Fig. 8), which is particularly time-saving and does not require chemical agents to remove the extra copper (Fig. 8.c). A milling machine (MIPEC 4MILL300ATC, [30]) was used to trim the desired antenna layout (Fig. 8.b) from a 35 μm thick adhesive sheet of copper temporarily laid over a wooden support (Fig. 8.a). Then, after the Magnus-S3 IC was mounted with a conductive paste (Fig. 8.d), the antenna could be easily transferred to the flexible sheets (Fig. 8.e-g).

The manufacturing steps for assembling the epidermal device were then as in Fig. 9. It is worth noticing that the encapsulation performed by means of the medical plaster sheets is such that the final device is fully sealed with respect to the skin and the environment (Fig. 9.g). Moreover, the protective film on the adhesive side of the Fixomull® layer closest to the skin (Fig. 9.h) is not removed until use. In this way, the sterility of the patch at the time of application is guaranteed.

B. Prototype

The overall thickness of the resulting prototype (Fig. 9.g,h) is 0.5 cm and the overall diameter is 4.4 cm (plus the extra Fixomull® that exceeds the size of the device for adhesion to the skin). The footprint is comparable with state-of-the-art DHF thermometers [21], but the proposed device is much lower-profile (i.e., 0.5 cm thick with respect to 1.5 cm [21]) so that it is more similar to a medical patch. Moreover, it is breathable, soft, and flexible (Fig. 9.i). Finally, unlike the plaster, which is disposable, the core ensemble of the device (i.e., biosilicone layers and loop modules) can be removed and re-used several times with new plasters.

V. Experimental Characterization

A. Electromagnetic Performance

The electromagnetic characterization of the multi-point flexible sensor was performed in a semi-anechoic space by means of a wideband circularly polarized (CP) antenna connected to the UHF Tagformance Pro station by Voyantic [31]. The CP interrogation can simultaneously activate all the ICs regardless of the mutual orientation between the device and the interrogator [12]. The device under test was placed 10 cm away from the antenna, in the broadside direction, and attached to a semi-solid three-layers phantom by AET [32] (Fig. 10.a) having the same size and nominal parameters of the above numerical phantom. In a separate test, the sensor was also worn by a volunteer on the upper left side of the chest at the subclavicular region (Fig. 10.b).

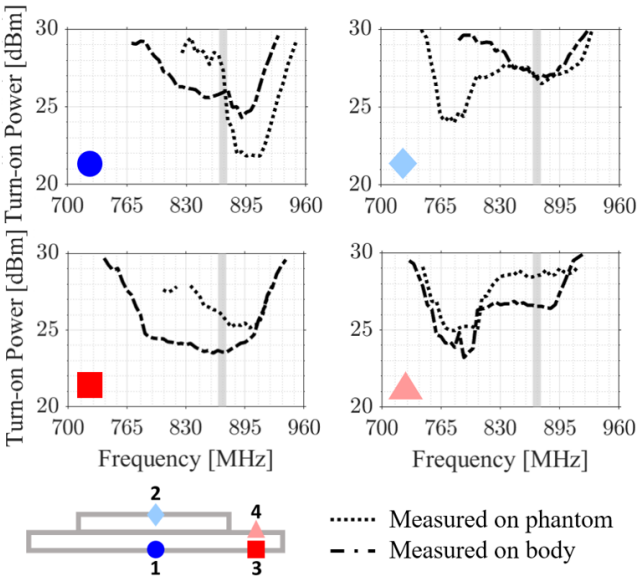

Fig. 11. Measured trends of the turn-on powers along the broadside over frequency of the four loops of the device, on both the electromagnetic phantom and the human body. Shadowed x-line indicates the European UHF band.

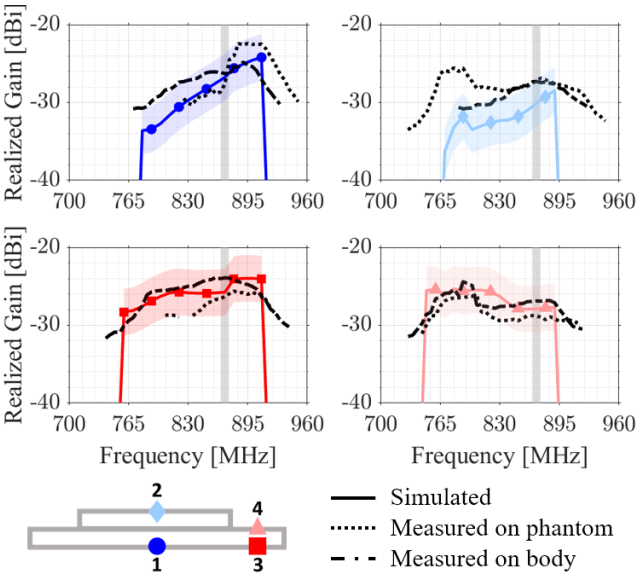

Fig. 12. Measured trends of the realized gains along the broadside over frequency of the four loops of the device, on both the electromagnetic phantom and the human body. Comparison with simulated results (solid lines with shadowed $\pm 3\ dBi$ uncertainty regions). Shadowed x-line indicates the European UHF band.

Fig. 11 shows the measured turn-on powers referred to the four antennas when the device was placed on the phantom and the body. The mutual difference is negligible in the UHF band. Fig. 12 shows the corresponding realized gains, calculated as in [33], and compared with the simulated data. Few frequency shifts occur with respect to the simulations, probably due to manufacturing imperfections, phantom properties degradation, and unclear human properties. Nevertheless, thanks to the

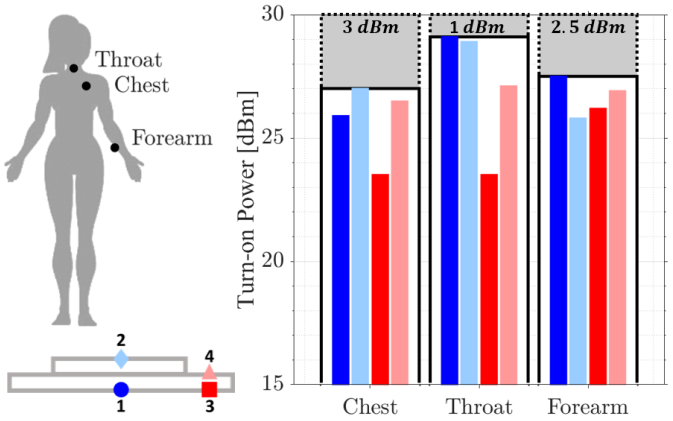

Fig. 13. Measured turn-on powers of the four antennas when the device is placed on three different body districts having different curvatures. Grey regions indicate the power margins with respect to 30 dBm maximum source power from the reader. Frequency fixed at 870 MHz.

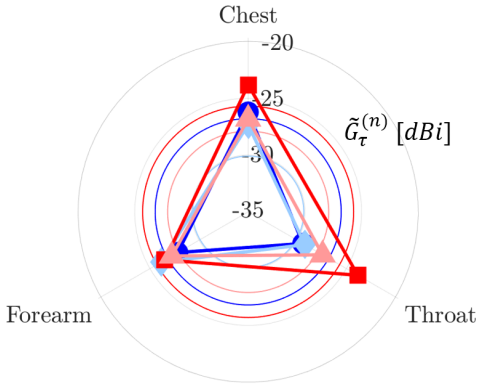

Fig. 14. Measured realized gains $\tilde{G}_\tau^{(n)}$ of the four antennas when the device is placed on three different body districts having different curvatures. Frequency fixed at 870 MHz. Circle lines indicate the four ICs' realized gain estimated from simulations. Legend as in Fig. 13

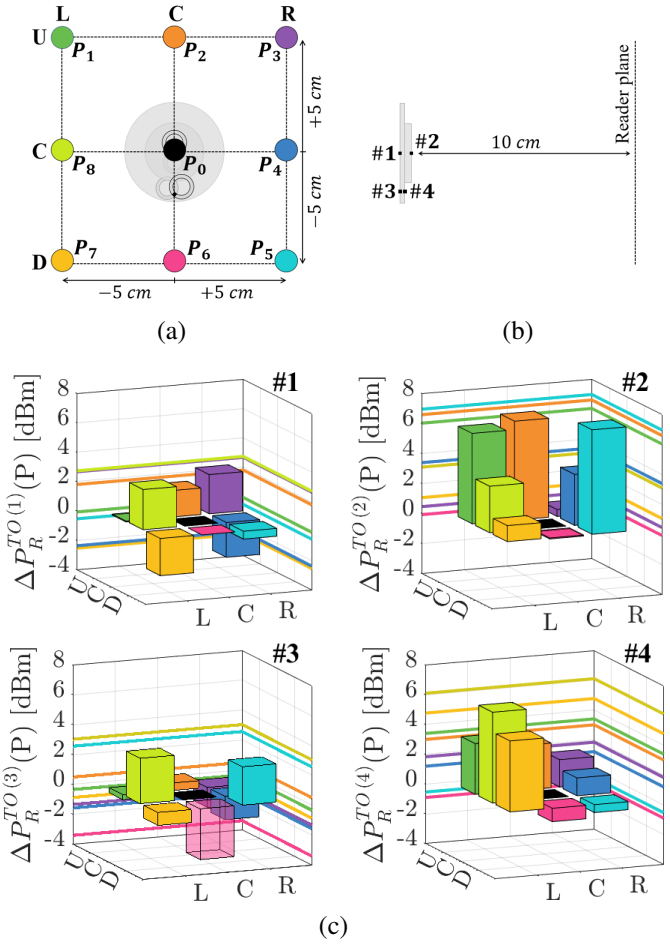

Fig. 15. Measurements of the effect of device-reader misalignment. (a) Front and (b) side view of the tested reader positions with respect to the worn device. The colored circles indicate the center of the reader antenna, always placed 10 cm from the device. Dimensions are in scale. (c) Differential turn-on power $\Delta P_R^{TO\,(n)}(P) = P_R^{TO\,(n)}(P_0) - P_R^{TO\,(n)}(P_i)$ for each n-th antenna, for each considered position $i = \{1, ..., 8\}$. Frequency fixed at 870 MHz.

auto-tuning, the response is quite stable in a very wide frequency band, so that these shifts can not affect the overall performance. Most importantly, both kinds of measurements are reasonably in agreement with the simulations, and hence the expected communication performance is confirmed. , although the power margins are overall limited (i.e., turn-on powers quite high), the estimated read distance for all the nodes is $\{18, 22\}\,cm$ for the on-phantom and on-skin measurements, respectively.

B. Impact of Device Curvature on the Radiation Performance

An experimental evaluation of the capability of the multi-point sensor to robustly transmit the data collected by the four ICs was performed when the device was placed on different parts of the human body having different curvatures. In particular, the chest, the throat, and the medial forearm (Fig. 13) of a volunteer (age 29, height 155 cm, weight 58 kg) were considered. The corresponding curvatures were $\{0,\ 0.2,\ 0.5\}$ cm^{-1}. Due to the effect of bending, the boundary conditions seen at the ports of the antennas change and, above all, the relative position between the four antennas inside the device changes. As a consequence, the ICs may require different turn-on powers to activate (Fig. 13). The chest position actually seems to be the most convenient as it requires the lowest turn-on power to activate all the ICs (yet similarly to the forearm), and accordingly it has the maximum power margin (grey region). The overall power margin is evaluated by (4) for each considered placement over the body with respect to the highest turn-on power of the four ports. It is equal to 3 dBm for chest and forearm, and just 1 dBm for the throat.

Fig. 14 shows the corresponding realized gains of the four antennas in the considered positions, and compared to the simulated data. The electromagnetic performance is just slightly affected by the bending, with limited variations of ± 1.5 dBi with respect to the average realized gains. This means that the flexibility of the device can be fully leveraged without sacrificing the performance. Moreover, very limited variations are also experienced by each IC with respect to the simulated results, meaning that the considered simplified electromagnetic layered phantom is overall adequate for the characterization of the four-loop device.

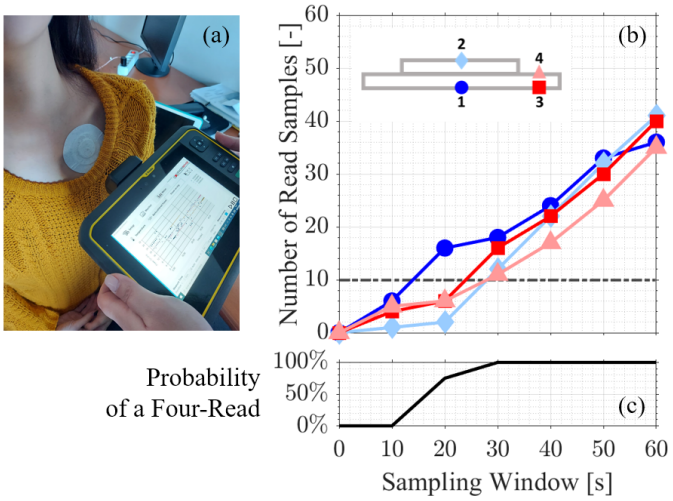

Fig. 16. (a) Measurement setup for the readability test: hovering a hand-held reader at a distance of $10 \pm 2\,cm$ from the device. (b) Number of readings of each sensor for each considered measurement duration. Dashed, the minimum required samples. (c) Probability of having a four-read for each considered measurement duration.

C. Effect of Device-Reader Misalignment

The capability of the multi-point sensor to robustly transmit the data collected by the four ICs was experimentally evaluated when the reader antenna is not perfectly aligned to the device. This could be the case of realistic use-case scenario, such as that of an operator that occasionally interrogates the device using a hand-held reader.

The distance between the device and the reader antenna was kept fixed at $10\,cm$ while shifting the center of the antenna $\pm 5\,cm$ up/down and left/right with respect to the center of the device (Fig. 15.a,b). The differential turn-on power $\Delta P_R^{TO\,(n)}(P) = P_R^{TO\,(n)}(P_0) - P_R^{TO\,(n)}(P_i)$ was computed for each misalignment $P_{i=\{1,\ldots,8\}}$ with respect to the perfect alignment P_0 (Fig. 15.c). Since $\Delta P_R^{TO\,(n)}(P) < 0$ in only 28% of the cases, it follows that just a few positions require more power than the central one (P_0), while instead hovering the reader antenna around the normal axis of the device can ease the practical reading rather than hinder it.

D. Estimation of Sensing-oriented Reading Time

The estimation of core temperature in (1) requires that the temperature data are collected from all the four ICs simultaneously. Moreover, each measurement should return four temperature data $T_{1\text{-}4}$ given by the average over a specific time window in which at least 10 samples are collected [24]. A readability test was hence performed to evaluate the recommended duration of a measurement of the DHF thermometer and the corresponding probability of having a four-read. Firstly, the same scheduled measurement was repeated 6 times with progressively longer duration (from $10\,s$ to $60\,s$ with $10\,s$ steps) at a sampling rate of $1\,Hz$. In each measurement, a hand-held reader (Trimble® Yuma 7) was brought close to the device at a distance of $10 \pm 2\,cm$ and was hovered around its normal axis (Fig. 16.a) while the volunteer (age 27, height $164\,cm$, weight $47\,kg$) was sitting.

Fig. 16.b returns the number of readings of each IC for each considered measurement duration. At least $30\,s$ of reading are hence required to collect 10 samples from each sensor. Indeed, by repeating each measurement 20 times, the probability of having a four-read (i.e., at least 10 samples for each IC) is 75% and 100% for measurement durations of $20\,s$ and $30\,s$, respectively.

VI. Conclusion

The paper presented a multi-point epidermal temperature sensor that combines, for the first time, the DHF method with the flexible epidermal UHF RFID approach, to enable the non-invasive wireless monitoring of core body temperature from the skin.

The main strengths of the proposed device are its conformability to the human body and the wireless data collection. Indeed, the overall footprint of the RFID-based device is notably reduced with respect to the state-of-the-art (i.e., thickness of $0.5\,cm$ whit respect to $1.5\,cm$ [21]), and, more importantly, its comfort is notably improved since it is now flexible, soft, and similar to a medical patch. Finally, the experimental characterization proved the robustness of the communication link regardless of the effect of device flexibility and of real-life usage. Despite the reading distance is modest (i.e., $15\,cm$), the device is compatible with readings by a hand-held portable reader or a wearable on-body reader in close proximity.

Further efforts will be devoted to the assessment of the thermal data that the device can record under variable boundary conditions, in comparison with clinical golden standards.

References

[1] M. Sund Levander and E. Grodzinsky, "Assessment of body temperature measurement options," *British Journal of Nursing*, vol. 22, pp. 882–888, August 2013.

[2] D. Moran and L. Mendal, "Core temperature measurement: Methods and current insights," *Sports medicine (Auckland, N.Z.)*, vol. 32, pp. 879–85, February 2002.

[3] N. Taylor, M. Tipton, and G. Kenny, "Considerations for the measurement of core, skin and mean body temperatures," *Journal of Thermal Biology*, vol. 46, October 2014.

[4] K.-I. Kitamura, X. Zhu, W. Chen, and T. Nemoto, "Development of a new method for the noninvasive measurement of deep body temperature without a heater," *Medical Engineering Physics*, vol. 32, no. 1, pp. 1–6, January 2010.

[5] M. Huang, T. Tamura, W. Chen, and S. Kanaya, "Evaluation of structural and thermophysical effects on the measurement accuracy of deep body Thermometers based on dual-heat-flux method," *Journal of Thermal Biology*, vol. 47, November 2014.

[6] M. Huang, T. Tamura, Z. Tang, W. Chen, and S. Kanaya, "Structural Optimization of a Wearable Deep Body Thermometer: From Theoretical Simulation to Experimental Verification," *Journal of Sensors*, vol. 2016, pp. 1–7, December 2015.

[7] K. Saurabh, H. Rao, B. Amrutur, and S. Asokan, "Continuous Core Body Temperature Estimation Via Surface Temperature Measurements Using Wearable Sensors: Is it Feasible?" March 2014.

[8] J. Fang, Z. Congcong, and X. Ye, "Optimization of a Wearable Device for Core Body Temperature Monitoring Based on the Dual-Heat-Flux Model," *IOP Conference Series: Materials Science and Engineering*, vol. 677, December 2019.

[9] M. Huang, T. Tamura, Z. Tang, W. Chen, and S. Kanaya, "A Wearable Thermometry for Core Body Temperature Measurement and Its Experimental Verification," *IEEE Journal of Biomedical and Health Informatics*, vol. 21, pp. 1–1, February 2016.

[10] N. Panunzio and G. Marrocco, "SECOND SKIN Project: BioIntegrated Wireless Sensors for the Epidermal Monitoring and Restoring of Sensorial Injuries," in *2021 IEEE International Conference on RFID Technology and Applications (RFID-TA)*, October 2021, pp. 173–176.

[11] F. Camera, C. Miozzi, F. Amato, C. Occhiuzzi, and G. Marrocco, "Experimental Assessment of Wireless Monitoring of Axilla Temperature by Means of Epidermal Battery-Less RFID Sensors," *IEEE Sensors Letters*, vol. 4, no. 11, pp. 1–4, November 2020.

[12] C. Occhiuzzi, S. Parrella, F. Camera, S. Nappi, and G. Marrocco, "RFID-Based Dual-Chip Epidermal Sensing Platform for Human Skin Monitoring," *IEEE Sensors Journal*, vol. 21, no. 4, pp. 5359–5367, October 2020.

[13] N. Panunzio, G. M. Bianco, C. Occhiuzzi, and G. Marrocco, "RFID Sensors for the Monitoring of Body Temperature and Respiratory Function: a Pandemic Prospect," in *2021 6th International Conference on Smart and Sustainable Technologies (SpliTech)*, September 2021, pp. 1–5.

[14] C. Miozzi, F. Amato, and G. Marrocco, "Performance and Durability of Thread Antennas as Stretchable Epidermal UHF RFID Tags," *IEEE Journal of Radio Frequency Identification*, vol. 4, no. 4, pp. 398–405, June 2020.

[15] C. Miozzi, S. Amendola, A. Bergamini, and G. Marrocco, "Clinical Trial of Wireless Epidermal Temperature Sensors: preliminary results," in *EMBEC & NBC 2017*. Springer Singapore, June 2018, pp. 1041–1044.

[16] Axzon, "RFM3300-E Magnus-S3 M3E passive sensor IC," https://axzon.com/rfm3300-e-magnus-s3-m3e-passive-sensor-ic/, September 2021.

[17] EM Microelectronic, "EM4325- EPC and UHF ICs," https://www.emmicroelectronic.com/product/epc-and-uhf-ics/em4325, June 2022.

[18] N. Panunzio and G. Marrocco, "Flexible and Wireless Multi-Sensor Thermometer based on Dual-Heat-Flux Model," in *2022 IEEE 12th International Conference on RFID Technology and Applications (RFID-TA)*, September 2022, pp. 29–32.

[19] M. Wagih et al., "Microwave-Enabled Wearables: Underpinning Technologies, Integration Platforms, and Next-Generation Roadmap," *IEEE Journal of Microwaves*, November 2022.

[20] N. Panunzio, A. Diamanti, and G. Marrocco, "Flexible Multi-Layer Sensor for the Wireless Implementation of Dual-Heat-Flux Monitoring of Body Temperature," in *2022 IEEE International Conference on Flexible and Printable Sensors and Systems (FLEPS)*, June 2022, pp. 1–4.

[21] M. Huang and W. Chen, "Theoretical Simulation of the Dual-Heat-Flux Method in Deep Body Temperature Measurements," *Annual International Conference of the IEEE Engineering in Medicine and Biology Society*, vol. 2010, pp. 561–4, August 2010.

[22] W. Morton and W. Hearle, *Physical Properties of Textile Fibres*, 4th ed. Cambridge, UK: Woodhead Publishing, 2008.

[23] R. Salvado, C. Loss, R. Gonçalves, and P. Pinho, "Textile Materials for the Design of Wearable Antennas: A Survey," *Sensors*, vol. 12, no. 11, pp. 15 841–15 857, November 2012.

[24] F. Camera and G. Marrocco, "Electromagnetic-Based Correction of Bio-Integrated RFID Sensors for Reliable Skin Temperature Monitoring," *IEEE Sensors Journal*, vol. 21, no. 1, pp. 421–429, August 2021.

[25] M. C. Caccami and G. Marrocco, "Electromagnetic Modeling of Self-Tuning RFID Sensor Antennas in Linear and Nonlinear Regimes," *IEEE Transactions on Antennas and Propagation*, vol. 66, no. 6, pp. 2779–2787, March 2018.

[26] G. Marrocco, "RFID Grids: Part I - Electromagnetic Theory," *IEEE Transactions on Antennas and Propagation*, vol. 59, no. 3, pp. 1019–1026, January 2011.

[27] N. Panunzio and G. Marrocco, "A Multi-port Formulation for Electromagnetic Coupled Auto-tuning RFID Antennas," in *2021 XXXIVth General Assembly and Scientific Symposium of the International Union of Radio Science (URSI GASS)*, September 2021, pp. 1–4.

[28] N. Panunzio, E. Fontana, F. Montecchia, and G. Marrocco, "Two-channel Epidermal RFID Sensor for the Wireless Bilateral Analysis of Nasal Respiration," *IEEE Sensors Journal*, pp. 1–1, October 2022.

[29] ETSI EN 300 220-2 V3.2.1 (2018-06), "Short Range Devices (SRD) operating in the frequency range 25 MHz to 1000 MHz," https://axzon.com/rfm3300-e-magnus-s3-m3e-passive-sensor-ic/, December 2021.

[30] MIPEC, "PCB milling machine 4MILL300ATC - automatic tool change," https://www.webshop.mipec.eu/PCB-milling-machine-4MILL300ATC-automatic-tool-change-d71.htm?tab=description, July 2022.

[31] Voyantic, "Tagformance Pro," https://voyantic.com/products/tagformance-pro, September 2021.

[32] AET, "Human Body Equivalent Phantom in Low-Frequency, Microwave, and Millimeter-Waves," https://www.aetassociates.com/hard_detail.php?phantom0, July 2022.

[33] N. Panunzio, F. Ciafrei, C. Magnante, G. M. Bianco, and G. Marrocco, "Sensorized Facemask with Temperature RFID Sensor for Cough Analysis," in *2022 16th European Conference on Antennas and Propagation (EuCAP)*, April 2022, pp. 1–5.

Nicoletta Panunzio (Student Member, IEEE) received the B.S. and M.S. degrees (Hons.) in Medical Engineering from the University of Rome Tor Vergata, Rome, Italy, in 2017 and 2020, respectively. She is currently pursuing the Ph.D. degree in Computer Science, Control, and Geoinformation within the Pervasive Electromagnetics Lab at the same university.

She serves as a teaching tutor in two courses within the Medical Engineering School (Mechanics of Biological Systems and Wearable Systems and Medical Telemetry), and as a Delegate Professor in a course within the Engineering Sciences School (Electromagnetic Fields). Her research interests include on-skin flexible antennas for smart health monitoring and detection of biophysical parameters, with a particular interest in innovative multipoint systems to strengthen sensing accuracy and enable multiparametric sensing.

Ms. Panunzio's awards and honors include the Best Student Paper Award (2021 IEEE International Conference on RFID Technology and Applications) and the Best Paper Award (2022 Seventh International Conference on Smart and Sustainable Technologies).

Arianna Diamanti was born in Rome in 1992. She received the M.S. degree in Medical Engineering from the University of Rome Tor Vergata, Rome, Italy in 2022 with a Master thesis about flexible dual-heat-flux wireless sensors for measuring body temperature.

She is currently with the Microwave Vision Group (MVG), Rome, Italy within the Antenna Design R&D group.

Gaetano Marrocco (Senior Member, IEEE) received the M.S. degree in Electronic Engineering and Ph.D. degree in Applied Electromagnetics from the University of L'Aquila, L'Aquila, Italy in 1994 and 1998, respectively. He was a Researcher at the University of Rome Tor Vergata, Rome, Italy from 1994 to 2014. He was an Associate Professor of Electromagnetics from 2013 to 2017, and a Full Professor at the University of Rome Tor Vergata since 2018. He currently serves as Director of the Medical Engineering School.

The first phase of his career was devoted to the research on Time-Domain Electromagnetics with application to structural, broadband, and ultra-wideband antennas for Satellite (ESA, ASI), Avionic, and Naval (Leonardo) communications. Then, since 2002, he is investigating sensor-oriented miniaturized antennas for Biomedical Engineering and Radiofrequency Identification (RFID), contributing to the move from the RF labeling of objects to the passive sensor networks in the Internet of Things era. He carried out pioneering research on body-centric battery-less wireless sensors concerning textile RFID antennas, tattoo-like sensors (flexible and stretchable epidermal electronics), and radio-sensors embedded inside implanted prostheses.

He serves as Associate Editor for the IEEE Journal of Radiofrequency Identification and for the IEEE Journal of Flexible Electronics and was a member of the IEEE Antennas and Propagation Society Awards committee. Moreover, he is the chair of the Italian delegation URSI Commission D Electronics and Photonics. He was the chair of the Local Committee of the V European Conference on Antennas and Propagation (EUCAP-2011), TPC chair of the 2012 IEEE-RFID TA in Nice, France, TPC track-chair of the 2016 IEEE Antennas and Propagation Int. Symposium, TPC track-chair of IEEE-RFID 2018-22, USA.

Prof. Marrocco is the director of the Pervasive Electromagnetics Lab (www.pervasive.ing.uniroma2.it) and the co-founder and president of the University spin-off RADIO6ENSE (www.radio6ense.com), which is active in the short-range electromagnetic sensing for the Industrial Internet of Things, Smart Manufacturing, Automotive and Medical Device.

He is listed in the PLOS ranking of Top 2% Scientists Worldwide (source Univ. Stanford, 2022).